Editors' Suggestion

Reduced crystal symmetry as the origin of the ferroelectric polarization within the incommensurate magnetic phase of $TbMn_2O_5$

N. Narayanan,[1,2] P. J. Graham,[3] P. Rovillain,[2,3,4] J. O'Brien,[3] J. Bertinshaw,[3,5] S. Yick,[2,3] J. Hester,[2] A. Maljuk,[6,7] D. Souptel,[7] B. Büchner,[7,8] D. Argyriou,[6,9] and C. Ulrich[3,*]

[1]*School of Physical, Environmental and Mathematical Sciences, University of New South Wales, Canberra, Australian Capital Territory 2600, Australia*

[2]*The Australian Centre for Neutron Scattering, Australian Nuclear Science and Technology Organisation, Lucas Heights, New South Wales 2234, Australia*

[3]*School of Physics, University of New South Wales, Sydney, New South Wales 2052, Australia*

[4]*Sorbonne Université, CNRS, Institut des NanoSciences de Paris, INSP, UMR7588, F-75005 Paris, France*

[5]*Max-Planck-Institut für Festkörperforschung, Heisenbergstraße 1, D-70569 Stuttgart, Germany*

[6]*Helmholtz-Zentrum Berlin für Materialien und Energie, D-14109 Berlin, Germany*

[7]*Leibniz Institut für Festkörper- und Werkstoffforshung (IFW) Dresden, Helmholtzstraße 20, D-01069 Dresden, Germany*

[8]*Institut für Festkörper- und Materialphysik, Technische Universität Dresden, 01069 Dresden, Germany and Würzburg-Dresden Cluster of Excellence ct.qmat, Technische Universität Dresden, 01062 Dresden, Germany*

[9]*European Spallation Source ESS AB, S-22100 Lund, Sweden*

(Received 13 September 2021; accepted 19 January 2022; published 10 June 2022)

The precise crystal symmetry, and hence the emergence of the electric polarization, still remains an open question in the multiferroic RMn_2O_5 (R = rare earth, Bi, Y). While previous diffraction studies have indicated the centrosymmetric space group *Pbam*, an atomic displacement allowing for electric polarization would require a noncentrosymmetric crystal symmetry. Our single crystal neutron diffraction experiments on $TbMn_2O_5$ provide direct evidence of a reduced crystallographic symmetry with the polar space group $P12_11$ already above the multiferroic phase transition, indicating that a symmetric $\mathbf{S_i} \cdot \mathbf{S_j}$ spin coupling, i.e. magnetostriction is the dominating mechanism in the commensurate magnetic phase. Furthermore, the commensurate magnetic reflections are in accordance with a quartile step spin spiral along the c axis. Therefore, the antisymmetric $\mathbf{S_i} \times \mathbf{S_j}$ exchange via the inverse Dzyaloshinskii-Moriya interaction contributes as well and becomes the leading term in the low-temperature incommensurate spin-spiral magnetic phase. These findings provide important information for the understanding of the complex interplay between magnetic and structural order throughout the multiferroic RMn_2O_5 series.

DOI: 10.1103/PhysRevB.105.214413

I. INTRODUCTION

The coexistence of both ferroelectricity and magnetism in multiferroic materials offers new possibilities in developing novel data storage and sensor technologies with advanced functionalities since both ordered components can be exploited simultaneously [1–5]. In type-II multiferroics, both properties can even be switched by each other, which is known as the magnetoelectric (ME) effect. The direct control of magnetic components in memory storage devices through electric manipulation can provide faster storage and retrieval of information and has the potential to increase the data storage capacity by five to six orders of magnitude [3]. However, due to the complex spin and charge interactions in these systems, the underlying quantum mechanical processes behind these phenomena are still not fully understood. Although there is a general understanding of this phenomenon, some unsettled discussion remains concerning the role of ionic displacements, and the lattice in general, in influencing the ME coupling in a number of multiferroic systems [4,5]. A more thorough understanding of the underlying conditions for ME coupling will thus provide valuable insight into multiferroic systems and further the progress in their applications.

The RMn_2O_5 series (R = rare-earth Pr–Lu, and Bi, Y) is a group of such multiferroic systems demonstrating a colossal ME effect that has so far attracted considerable efforts in scientific investigation [6–11]. While the electric polarization of around $45\,nC/cm^2$ is several orders of magnitude weaker as compared to regular ferroelectrics, its ME coupling is strong [12] and the direction of the electric polarization can even be reverted in a magnetic field applied along the crystallographic a direction [7]. Already in the 1960s Bertaut *et al.* [13,14] and Abrahams and Bernstein [15] determined that the space group of RMn_2O_5, with R = Ho, Bi, and Dy, respectively, is *Pbam* (#55 in the *International Tables for Crystallography* [16]). This space group was confirmed for the entire series of RMn_2O_5 [17–23] (for review, see [24,25]). The unit cell consists of four formula units and the lattice parameters of $TbMn_2O_5$ are $a = 7.3251(2)$ Å, $b = 8.5168(2)$ Å, and $c = 5.6750(2)$ Å at room temperature [20]. The corresponding crystallographic structure is shown in Fig. 1 and

*c.ulrich@unsw.edu.au

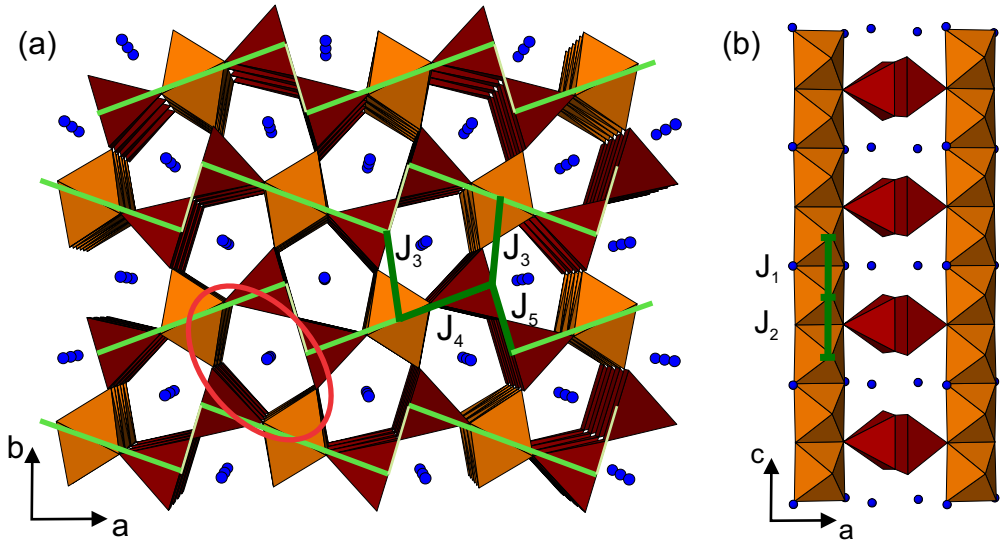

FIG. 1. Crystal structure of $TbMn_2O_5$ at room temperature (crystallographic data from Ref. [20]). (a) *ab* plane. The key elements are edge-sharing $Mn^{3+}O_5 - Mn^{4+}O_6 - Mn^{3+}O_5$ pyramid-octahedron-pyramid units which are linked to zigzag chains along the *a* direction (see light green lines). The red circle indicates the circular arrangement of five Mn^{4+}-Mn^{3+}-Mn^{3+}-Mn^{4+}-Mn^{3+} polyhedra, which are the origin of the spin frustration in $TbMn_2O_5$. (b) *ac* plane. Edge-sharing $Mn^{4+}O_6$ octahedral chains along the *c* direction are linked by two $Mn^{3+}O_5$ pyramids. The dark green lines in both panels indicate the magnetic exchange interactions J_1–J_5 in the *ab* and *ac* planes.

can be described as a network of edge- and corner-sharing $Mn^{4+}O_6$ octahedra (Mn^{4+}: $3d^3$; $S = 3/2$ at the Wyckoff position 4*h*) and base-centered $Mn^{3+}O_5$ square pyramids (Mn^{3+}: $3d^4$; $S = 2$ at the Wyckoff position 4*f*). Along the *c* axis the $Mn^{4+}O_6$ octahedra form edge-sharing chains which are linked by $Mn^{3+}O_5$ pyramid pairs. The *ab* plane is dominated by $Mn^{3+}O_5$-$Mn^{4+}O_6$-$Mn^{3+}O_5$ corner-sharing (Mn^{3+}-Mn^{4+}-Mn^{3+}) units, which form zigzag chains in the *a* direction (see light green lines in Fig. 1), and which are weakly connected along the *b* direction. From another perspective, five $Mn^{3+/4+}$ polyhedra (two octahedra and three pyramids) are forming a circular arrangement in the *ab* plane with the sequence Mn^{4+}-Mn^{3+}-Mn^{3+}-Mn^{4+}-Mn^{3+} (see red circle in Fig. 1). Since all nearest neighbor interactions are antiferromagnetic, this five-spin structure can be considered as the origin of the geometrical spin frustration in the compounds RMn_2O_5.

Five antiferromagnetic superexchange interactions J_1–J_5 are responsible for the magnetic order in the series RMn_2O_5 (see dark green lines in Fig. 1). These interactions were already identified by Abrahams and Bernstein in 1967 [15] and are labeled according to the notation given in the literature [11,15,17,22,23]. The J_1 and J_2 exchange interactions couple the spins of the Mn^{4+} ions within the one-dimensional chain along the *c* axis; J_1 is at the level of the Tb^{3+} layers and J_2 is connected through the $Mn^{3+}O_5$ pyramidal layers. As a consequence, the J_2 magnetic interaction is competing with J_3 and J_4 which leads to the incommensurate magnetic order along the *c* axis. The exchange interaction J_4 acts within the Mn^{3+}-Mn^{4+}-Mn^{3+} units of the zigzag chains in the *ab* plane. J_3 connects the zigzag chains in the *b* direction by a $Mn^{4+} - Mn^{3+}$ superexchange interaction through pyramidal basal corners, while J_5 connects the Mn^{3+}-Mn^{4+}-Mn^{3+} units antiferromagnetically in the *a* direction through the pyramidal basal-basal Mn^{3+}-Mn^{3+} ions. In the case of the centrosymmetric crystal structure *Pbam*, J_3 is degenerate. An atomic displacement of the Mn^{3+} or Mn^{4+} ion in the *ab* plane would lift this degeneracy and lead to two different J_3 and J_4 interactions, respectively [6,22]. According to theoretical first-principles calculations [24,25] and inelastic neutron scattering experiments on YMn_2O_5 and $TbMn_2O_5$ [26,27], J_4 and J_5 are the leading contributions. These interactions are responsible for the antiferromagnetic arrangement of the spins in the zigzag chains, which are weakly coupled through J_3 in the *b* direction. In the case of a magnetic rare-earth ion, additional exchange interactions between the R^{3+} ions and between the R^{3+} and Mn^{3+} and Mn^{4+} ions are present. However, since the phase diagram of the RMn_2O_5 series shows a universal behavior independent of the magnetic nature of the R^{3+} ions [10,11], the R^{3+} ions have only a minor influence on the magnetic structure of the Mn sublattice and would only become relevant at low temperatures.

Due to the different competing magnetic interactions caused by geometrical frustration, $TbMn_2O_5$ possesses several magnetic phases with both commensurate (CM) and incommensurate (ICM) spin arrangements [17,22,23,28]. The onset of the antiferromagnetic order occurs at $T_{\text{HT-ICM}} = 42$ K to the high-temperature incommensurate magnetic phase (HT-ICM), which is characterized by the magnetic propagation vector $\mathbf{q}_{\text{HT-ICM}} = (\frac{1}{2}-\delta_x, 0, \frac{1}{4}+\delta_z)$. The values of δ_x and δ_z decrease continuously with temperature; i.e., the magnetic propagation vector $\mathbf{q}_{\text{HT-ICM}}$ changes from (0.487, 0, 0.276) to (0.496, 0, 0.262) [6,17,19,22,23,28,29]. A commensurate magnetic (CM) structure is formed at $T_{\text{CM}} = 37.8$ K, where the magnetic propagation vector locks in to the value of $\mathbf{q}_{\text{CM}} = (\frac{1}{2}, 0, \frac{1}{4})$. This phase transition is accompanied by the onset of an electric polarization along the *b* axis [7,12]. Below $T_{\text{LT-ICM}} = 22.4$ K the magnetic structure becomes incom-

mensurate again (low-temperature incommensurate phase, LT-ICM). At this phase transition the electric polarization drops almost to zero and then increases slightly upon further cooling. The components q_x and q_z of the magnetic propagation vector change continuously and reach a stable value of $\mathbf{q}_{\text{LT-ICM}} = (0.488, 0, 0.313)$ below $T \sim 16\,\text{K}$. Finally, at $T_{\text{Tb}} = 9\,\text{K}$ the Tb^{3+} moments order magnetically and the electric polarization increases strongly.

In the *ab* plane the spins of $TbMn_2O_5$ are oriented antiferromagnetically. Their direction is predominantly within the *ab* plane with a weak canting of the spins out of plane [22,23,29]. They are pointing almost perfectly along the direction of the $Mn^{3+} - Mn^{4+} - Mn^{3+}$ polyhedral units of the zigzag chains; i.e., they possess an angle to the *a* axis of 10 ° (14 °) for the Mn^{3+} spins and 24 ° (11 °) for the Mn^{4+} according to Chapon *et al.* [22] and Blake *et al.* [23] (in brackets). This holds for all magnetic phases, the HT-ICM, CM, and LT-ICM phases. At low temperature the Tb^{3+} moments induce a further rotation of Mn^{3+} and Mn^{4+} spins away from the *a* axis. The Tb^{3+} spins are almost parallel to the Mn^{3+} spins and antiferromagnetically arranged in a "– + + –" sequence in the *ab* plane [6,23,29]. Already in 1973, Buisson described the spin structure of the rare-earth series RMn_2O_5 with $R =$ Lu, Er, Y, Ho, Tb, and Nd as helical [17]. Recent neutron diffraction experiments on RMn_2O_5 with $R =$ Y, Tb, Ho, Er, and Bi have indicated that a spin spiral exists also in the *bc* plane with a propagation direction along the *c* axis and a $\pi/2$ phase shift, i.e., a spin quadrature in the CM phase and close to $\pi/2$ phase steps in the high-temperature and low-temperature ICM phases [29–37].

In contrast to multiferroics such as $TbMnO_3$ and $DyMnO_3$ [38–40], the strongest electric polarization in the RMn_2O_5 series appears in the CM phase and not the ICM phases. This seems to be in contradiction to the model of ferroelectricity induced by magnetic chirality [41,42]. The existence of electric polarization in the commensurate magnetic phase raises the question about the responsible microscopic mechanism. In general, two models have been proposed for the magnetoelectric coupling: (i) ferroelectric polarization through atomic displacements caused by magnetic exchange striction and (ii) ferroelectricity induced by a spin spiral. In the case of the magnetic exchange striction the symmetric Heisenberg exchange interaction causes a displacement of the Mn^{3+} or Mn^{4+} ions. Quantitatively the magnitude of the electric polarization is proportional to the scalar product of $\mathbf{S_i} \cdot \mathbf{S_j}$ [6,22,23,43–45]. The noncollinearity is not essential in this case and the stacking order along the *c* axis is irrelevant. In the spin-spiral model the ferroelectricity is generated through magnetic chirality [41,42]. A spin spiral can be caused by the spin orbit driven antisymmetric Dzyaloshinskii-Moriya interaction. A spin current, which is induced by the spin spiral, generates an electric polarization $\mathbf{P} \propto \mathbf{r_{ij}} \times (\mathbf{S_i} \times \mathbf{S_j})$, where $\mathbf{r_{ij}}$ is the propagation direction of the spin spiral [4,41]. It is important to note that in the case of a spin current, atomic displacements are not necessarily required, and the electric polarization can arise entirely from orbital polarizations. In the case of the RMn_2O_5 series, the propagation direction of the spin spiral is along the *c* direction and the spins are rotating in the *bc* plane. Hence, the cross product between $\mathbf{S_i}$ and $\mathbf{S_j}$ is pointing along the *a* direction and the induced electric polarization is along the *b* direction. Since a spin spiral has been identified in all magnetic phases, both in the CM as well as in the ICM phases, the spin-current model most likely contributes in all magnetic phases to the electric polarization. However, this does not explain why the strongest electric polarization occurs in the CM phase. Therefore, in the CM phase, considerable contributions to the electric polarization must come from magnetic exchange striction. However, due to symmetry considerations, ferroelectricity is formally forbidden in centrosymmetric, and hence nonpolar crystals [46] as in the case of the originally determined space group *Pbam*. Therefore, Kagomiya *et al.* [6] proposed through group-theoretical considerations that the symmetry is lowered to the noncentrosymmetric, polar space group $Pb2_1m$ (#26). This is achieved through an atomic displacement of either the Mn^{3+} or Mn^{4+} ions along the zigzag chains in the *ab* plane. The resulting electric polarizations would cancel out at the atomic level along the *a* direction, while they would add up along the *b* direction. Since the expected atomic displacements responsible for the breaking of the symmetry are on the order of 0.005 Å (see, e.g., $DyMnO_3$ and $TbMnO_3$ [40,47]), direct evidence using diffraction techniques is elusive.

Various experiments have been performed thus far to provide proof for the atomic displacements. Anomalies in the thermal expansion indicate the existence of a strong magnetostriction effect [48,49]. In their neutron diffraction experiments Chapon *et al.* [22] observed a significant increase of the thermal displacement parameters of the Mn^{3+} ions (see also Refs. [23,50,51]) while Wilkinson *et al.* [29] observed large thermal displacement parameters for the Mn^{4+} ions. This could be an indication for a displacement of either the Mn^{3+} or Mn^{4+} ions and hence a splitting of their sites into two. This is supported by Mössbauer spectroscopy through the observation of two different hyperfine sextets [52,53]. As a consequence the magnetic exchange interaction J_3 between the zigzag chains and J_4 within the zigzag chains in the *ab* plane would each split into two different interactions (see Fig. 1) [22]. This would partly lift the magnetic frustration and would contribute to stabilizing the magnetic structure. Further evidence for a change in crystal symmetry was provided by optical spectroscopy where an additional phonon mode was observed in infrared spectroscopy whose shift in phonon frequency and intensity scales with the square of the electric polarization [54]. A first crystallographic indication for a change in the space group towards a polar group allowing ferroelectricity was provided by Noda *et al.* [32] who performed single crystal x-ray synchrotron diffraction experiments on RMn_2O_5 with $R =$ Y and Tb. They observed additional fundamental Bragg peaks for $(h\ 0\ l)$ at *h*-odd positions, which are forbidden in *Pbam* (see Table I in the Appendix) and also structural modulations along the *a* and *c* axes. Due to the limited number of reflections, the refinement results are ambiguous and they proposed either the space group $Pb2_1m$ or $P12_11$ for the ferroelectric phase. A more recent paper with evidence for symmetry breaking was published by Balédent *et al.* [55] who performed single crystal x-ray synchrotron diffraction experiments on RMn_2O_5 with $R =$ Pr, Nd, Gd, Tb, and Dy at temperatures above the magnetic and ferroelectric phase transition. They observed additional Bragg peaks for $(h\ 0\ l)$ and $(0\ k\ l)$ at odd positions for *h* and *k*, which are

forbidden in *Pbam*. In combination with first-principles calculations, they proposed the noncentrosymmetric space group *Pm*, which allows for a displacement of the Mn^{4+} ions and O^{2-} ions in the *ab* plane. This can generate electric polarization along the *b* direction.

However, the mechanism of the magnetoelectric coupling in the series RMn_2O_5 is still not fully understood and questions remain about the final crystallographic structure or if a thus far unobserved spin canting, i.e., a noncollinearity exists in the CM phase. Therefore, we have performed high-resolution single crystal neutron diffraction experiments on $TbMn_2O_5$ at various temperatures in order to determine the precise crystallographic and magnetic structure for all the magnetic and ferroelectric phases. Compared to powder diffraction, single crystal diffraction experiments offer the advantage that (i) even the weakest Bragg reflection peaks can be observed, (ii) each Bragg reflection is independently observed instead of the multiplicity, and (iii) there is no ambiguity about their indexing. Through the extinction rules, our data provide direct evidence for the symmetry lowered polar space group $P12_11$. Simultaneously the temperature dependence of the magnetic structure was determined for each magnetic phase.

II. EXPERIMENTAL DETAILS

Temperature-dependent neutron diffraction experiments were performed on a $TbMn_2O_5$ single crystal. The $4 \times 3 \times 3\,mm^3$ single crystal was grown from $PbO\text{-}PbF_2 - B_2O_3$ flux in a Pt crucible similar to the method described in Ref. [56]. The crystal was oriented using the neutron Laue-diffraction instrument Joey (see Fig. S1 in the Supplemental Material [57]) and then measured on the high-flux neutron diffractometer Wombat [58] at the OPAL research reactor at ANSTO. The instrument Wombat utilizes a monolithic ^{3}He area detector bank that covers 120 ° in 2θ within the equatorial plane and ± 7.8 ° in μ out of the equatorial plane. A neutron wavelength of $\lambda \approx 2.41$ Å was selected for all experiments using a Ge monochromator at the (113) reflection, which offers the advantage that the second-order reflections are forbidden. However, weak third-order contaminations were observed and identified in the diffraction patterns. Reciprocal space maps in the (h k 0), (h 0 l), and (0 k l) planes were obtained with about 60 ° sample rotations of $\omega = 0.5°$ steps at the selected temperatures of 4.0, 28, 35, 40, and 50 K, i.e., in the LT-ICM, CM, HT-ICM, and in the paramagnetic (PM) phases. Additional temperature-dependent scans were performed using a narrower q range with an ∼25 ° sample rotation of $\omega = 0.25°$ steps to capture a sufficient number of magnetic and nuclear Bragg reflections in each measurement sequence. Refinements of the integrated intensities were carried out by using a least-squares fitting method of the program suite FULLPROF [59].

III. RESULTS AND DISCUSSION

Figure 2 shows the reciprocal space map (RSM) in the (h 0 l) plane obtained by neutron diffraction using the instrument Wombat at ANSTO. The intense ring structures originate from powderlike diffraction of aluminum from the sample holder and the cryostat. The sharp peaks arise from nuclear and magnetic Bragg reflections of $TbMn_2O_5$ for the different magnetic

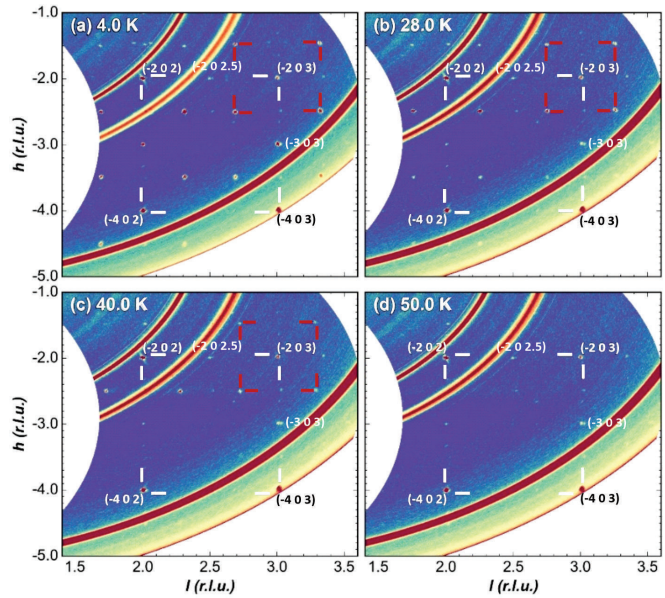

FIG. 2. Reciprocal space maps of $TbMn_2O_5$ in the (h 0 l) plane at various temperatures, i.e., at 4 K in the LT-ICM, at 28 K in the CM, at 40 K in the HT-ICM, and at 50 K in the PM phase. In the *Pbam* space group nuclear reflections appear at the position with $h = 2n$ and $l = n$ where n is an integer (see white right angles). Additional nuclear Bragg peaks are observed at (h 0 l) positions with h = odd integer and l = integer, and at (h 0 l) positions with h = integer and l = half-integer indices. The magnetic Bragg reflections at $(\frac{1}{2}-\delta_x, 0, \frac{1}{4}+\delta_z)$ are indicated by red right angles.

phases, i.e., the LT-ICM phase at 4 K, the CM phase at 28 K, the HT-ICM phase at 40 K, and the paramagnetic phase at 50 K. The nuclear Bragg reflections corresponding to the *Pbam* space group are indicated by white right angles and the magnetic Bragg peaks by red right angles. Allowed nuclear reflections in the space group *Pbam* appear at positions with $h = 2n$ and $l = n$ where n is an integer (see Table I in the Appendix). We observe additional weak reflections at (h 0 l) positions with odd h indices ($h = 2n + 1$) and l being an integer, and at (h 0 l) positions with integer h and half-integer l indices ($l = 0.5n$). The additional Bragg reflections cannot be attributed to λ/2 contaminations since a (113) oriented Ge monochromator was used to select the incident wavelength. However, λ/3 contaminations are possible. Weak reflections are visible for noninteger h and l values at (h 0 l) positions with $h = 1/3$ and $l = 1/3$ and are probably caused by λ/3 contaminations. However, λ/3 contaminations cannot account for the additional observed Bragg peaks at odd h positions, since for example, the corresponding Bragg peak (–9, 0, 6) which could cause the third-order peak at (–3, 0, 2) is forbidden in the space group *Pbam* and would hence be very weak for any symmetry lowered crystal structure. Therefore, the above listed additional Bragg reflections cannot be associated with any higher-order contaminations and must be caused by additional nuclear Bragg peaks, which would not be present for the *Pbam* crystal structure. This provides strong evidence that the crystal symmetry is lower than *Pbam*.

The additional structural Bragg peaks at (h 0 l) with h = odd integer, l = integer and h = integer, l = half-integer indices persist at all temperatures, i.e., throughout the LT-ICM,

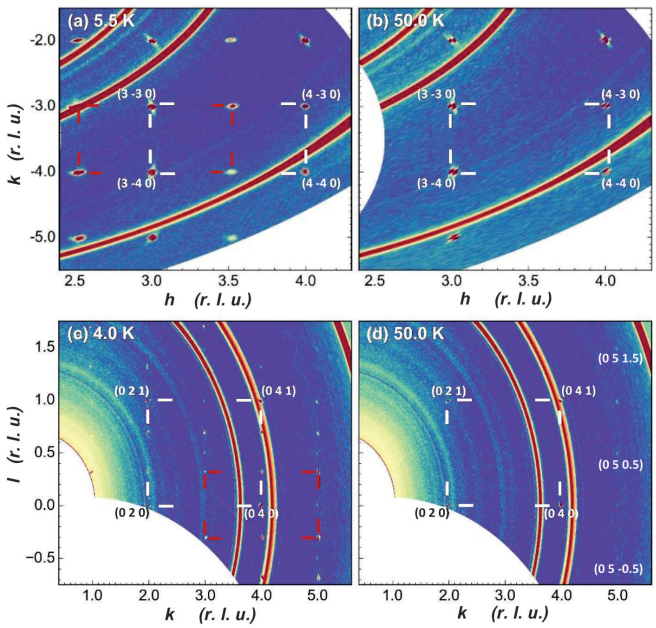

FIG. 3. (a,b) RSM of the hk plane of $TbMn_2O_5$ measured in the LT-ICM phase at 5.5 K and in the PM phase at 50 K. The nuclear Bragg reflections are highlighted by white right angles. At low-temperature out of plane magnetic Bragg peaks at $(h \pm 0.51, k, \pm 0.31)$ are also visible due to the vertical detector range of $\mu = \pm 7.8°$. (c,d) RSM of the kl plane at 4.0 K (LT-ICM phase) and at 50 K (PM phase). Additional nuclear Bragg peaks appear at both temperatures at half-integer l indices and are labeled underneath the reflection. In the LT-ICM phase at 4 K additional magnetic Bragg peaks appear. They can be attributed to out of plane reflections at $h = \pm 0.52$ and are indicated by red right angles.

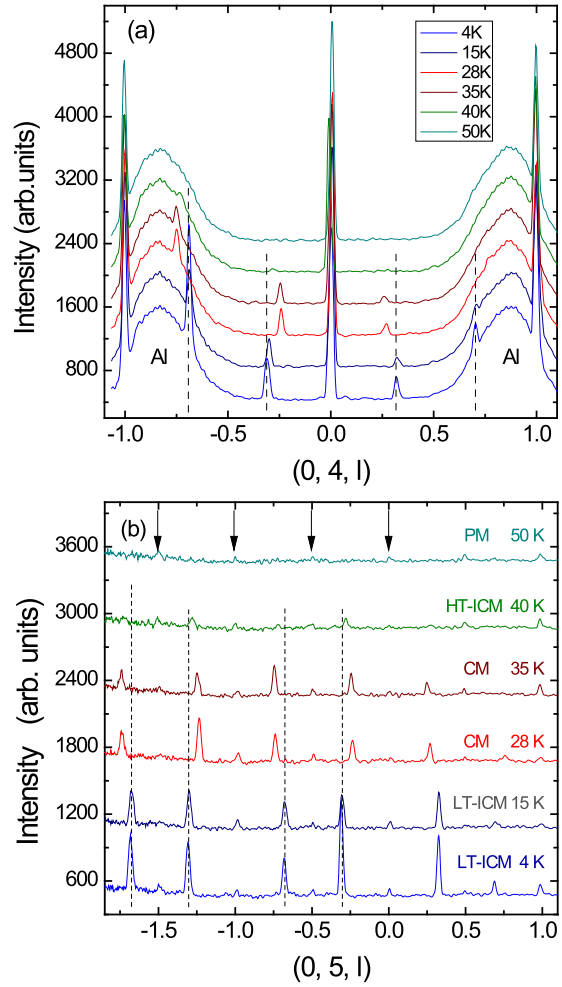

FIG. 4. Line cuts through the RSMs of the kl plane along the l direction, (a) along (0 4 l), and (b) along (0 5 l). The out of plane magnetic Bragg reflections at $(\pm 0.52, k, \frac{1}{4}+\delta_z)$ are indicated by vertical dashed lines. For the (0 5 l) direction, weak structural reflections are observed at l half-integer and l integer positions (see black arrows). They are present at all temperatures, also above the magnetic phase transition, and their intensity does not change with temperature.

CM, HT-ICM, and PM phases and their intensity remains almost constant at all temperatures. It is important to note that the additional nuclear Bragg reflections are already present at temperatures above the magnetic phase transition, which indicates that the crystal structure persists from high temperatures down to the lowest measured temperature. This is in agreement with Balédent *et al.* [55], who also observed additional Bragg reflections at room temperature in their single x-ray synchrotron diffraction experiments on RMn_2O_5 with R = Pr, Nd, Gd Tb, and Dy.

In order to obtain a complete overview, the RSMs of the (h k 0) and (0 k l) planes were measured as well. Figures 3(a) and 3(b) show the RSM of the hk plane taken at $T = 5.5$ K and 50 K, i.e., in the LT-ICM and PM phases, respectively. Nuclear Bragg peaks are observed at (h k 0) positions with h and k being an integer. Their intensity does not change with temperature as shown for the (3, −4, 0) reflection in Fig. S2 in the Supplemental Material [57]. These Bragg reflections are in accordance with the *Pbam* space group. At the lower temperature, i.e., in the LT-ICM phase, additional peaks appear at about half-integer h positions. They disappear above the magnetic phase transition and can therefore be attributed to magnetic scattering. Due to the vertical detector range of ±7.8 °, out of plane reflections with up to $l = \pm 0.36$ are also detected. Therefore, these Bragg peaks can be assigned to $(h \pm 0.51, k, \pm 0.31)$ magnetic reflections.

Figures 3(c) and 3(d) show the RSMs of the kl plane measured at 4 K in the LT-ICM phase and above the magnetic ordering temperature at 50 K. The nuclear Bragg reflections which are in accordance with the space group *Pbam* are highlighted by white right angles. Due to the vertical detector range of $\mu = \pm 7.8°$ out of plane magnetic Bragg peaks appear at the lowest temperature at $(\pm 0.52, k, \frac{1}{4}+\delta_z)$ in the kl plane (see red right angles). Figure 4 shows line cuts along the l direction extracted from the RSMs of the kl plane for the (0 4 l) and (0 5 l) directions, respectively. The out of plane magnetic Bragg reflections at $(\pm 0.52, k, \frac{1}{4}+\delta_z)$ are indicated by vertical dashed lines. They show the expected shift in position for the different magnetic phases from $l = 0.278$ in the HT-ICM phase to $l = 0.25$ in the CM phase and finally to $l = 0.31$ in the LT-ICM phase at the lowest temperature. It is important that we observe additional weak superstructure reflections at integer and half-integer l positions along, for example, the (0 5 l) line cut (see black arrows

in Fig. 4). They appear for even and odd integer k indices and are present in all magnetic phases and also above the magnetic phase transition. Note that the even integer k and half-integer l indices are hidden in Fig. 4(a) underneath the broad Al-powder lines, but are present in the kl plane RSM. This is accordance with the half-integer l indices observed in the RSM in the hl plane (see Fig. 2). In summary, besides the allowed nuclear Bragg reflections for the space group *Pbam*, additional structural Bragg peaks are observed at (h 0 l) and (0 k l) for odd-integer h and k indices. Further nuclear Bragg peaks are observed at half-integer l positions at (h, 0, 0.5l) and (0, k, 0.5l) with integer h or k values, respectively. They have not been observed before in the x-ray synchrotron diffraction experiments of Noda *et al.* [32] and Balédent *et al.* [55]. The appearance of the additional nuclear Bragg reflections, which are already present above the magnetic phase transition, indicates that the symmetry of $TbMn_2O_5$ must be lower than the previously determined space group *Pbam*.

In order to identify the crystal symmetry of $TbMn_2O_5$, we have performed an analysis of the extinction rules (reflection conditions) of the possible polar space groups and then modeled the integrated intensities for comparable space groups by performing least-squares refinements of the observed nuclear Bragg peaks. As the space group *Pbam* can be ruled out, we have considered the *translationsgleiche* subgroups of *Pbam*. Among them, $P2_1/c$ (#14) and $P2/m$ (#10) are centrosymmetric and $P2_12_12$ (#18) is piezoelectric. They are therefore not applicable. The remaining groups $Pc2a$ (#32) and $Pb2_1m$ (#26) are polar and allow electric polarization along b. However, the selection rules of our observed nuclear reflections violate three of four extinction rules for $Pc2a$. Furthermore, the appearance of odd integer k and integer l indices for (0 k l) violates the $k = 2n$ extinction rule of the space group $Pb2_1m$, which was previously suggested to be the symmetry-broken phase (see Table I in the Appendix). Therefore, the sub-subgroups have to be considered. Possible polar groups are Pm (#6), $P2$ (#3), Pc (#7), $P2_1$ (#4), and $P1$ (#1). The observed nuclear Bragg reflections again violate the (0 k l), $k = 2n$ extinction rule for the space group Pc. In order to determine the correct space group from the remaining four, the selection rule for the observed (0 k 0), $k = 2n$ nuclear Bragg peaks can be utilized. This additional condition is unambiguously fulfilled by $P2_1$ ($P12_11$) and rules out the remaining three space groups (see Table I in the Appendix). The polar space group $P12_11$ allows an electric polarization along the b direction and enables a doubling of the unit cell along the c direction, which explains the superstructure nuclear Bragg reflections at (h, 0, 0.5l) and (0, k, 0.5l) [see the irreducible representations (IRREPs) of $P12_11$ in Table II in the Appendix].

To further demonstrate the validity of the assignment to the space group $P12_11$, we have performed a refinement of the integrated intensities of the nuclear Bragg peaks within the commensurate phase measured at 28 K. The integrated intensities of all nuclear Bragg peaks were determined from the full measured RSMs of the hl, hk, and kl planes (note that Figs. 2 and 3 only show selected regions). For a comparison with the determined polar space group $P12_11$, we have chosen the centrosymmetric *Pbam* and the polar $Pb2_1m$ space groups, which

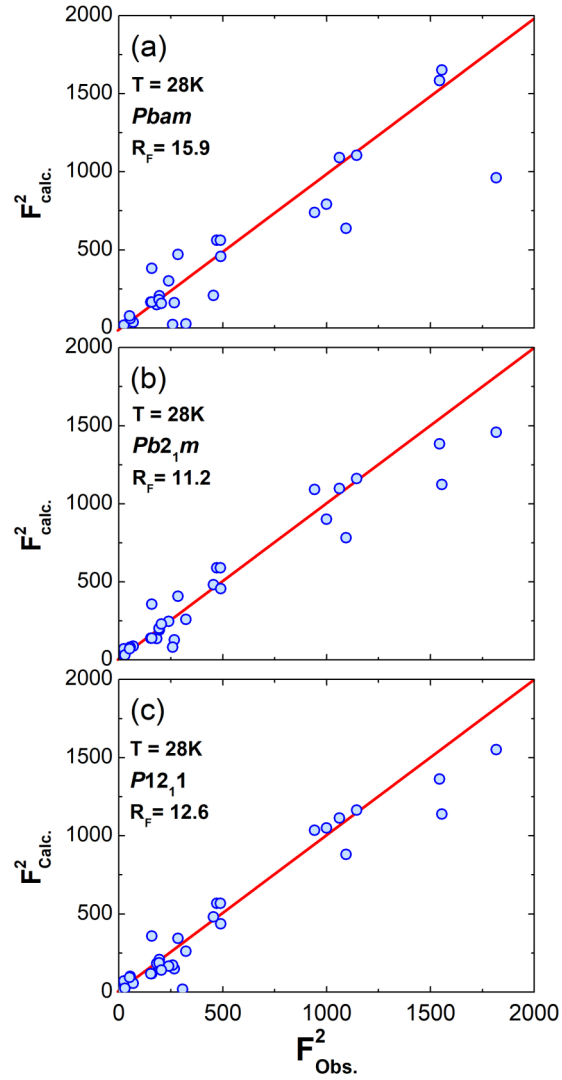

FIG. 5. Experimental and calculated integrated intensities of the fundamental nuclear Bragg reflections. The least-squares fitting method was applied to model the data taken at 28 K, i.e., in the CM phase of $TbMn_2O_5$. The results for the parent space group *Pbam* are shown in (a), for the polar space group $Pb2_1m$ in (b) and the designated polar space group $P12_11$ in (c).

were suggested in the literature before. Only the symmetry allowed reflections were considered for the least-squares fits with 26 independent reflections being available for the space group *Pbam*, 31 reflections for $Pb2_1m$, and 35 reflections for $P12_11$. The refinements were performed by least-squares fits using the FULLPROF program suite [59]. Figure 5 shows the comparison between the calculated and observed intensities for the three considered crystal structures. For the space group *Pbam* a residual value of $R(F) = 15.9$ was obtained. Considerable improvement of the $R(F)$ value was obtained for the polar group $Pb2_1m$ with $R(F) = 11.2$. However, as pointed out above, this space group does not allow the observed (0 k l) nuclear Bragg reflections with odd k and integer l indices. For the polar group $P12_11$ a slightly higher $R(F)$ value of 12.6 was obtained. However, this space group gave the most realistic description of the crystal symmetry of $TbMn_2O_5$ with respect to the selection rules. For this space group the superstructure

nuclear Bragg reflections along the c direction were also taken into account through displacement modulations. For simplicity the superspace formalism was avoided and instead the irreducible representation of $P12_11$ for the modulation vector $\mathbf{k_N} = (0, 0, \frac{1}{2})$ (little group) was used to determine the basis functions corresponding to the polar vector type distortions (see Table II in the Appendix). The best refinement of the structural modulation distortions was achieved for the IRREP Γ_2. In this case the structural modulation allows both Mn^{3+} and Mn^{4+} displacements and also O^{2-} distortions along the c direction and Tb^{3+} displacements along the a direction. The coordinate system transformation matrices from the space group $Pbam$ to $P12_11$ and the Wyckoff splitting of the ionic positions for the three considered space groups are given in Table T1 and T2 in the Supplemental Material [57], respectively.

The selection rules and the results of the refinements shown in Fig. 5 confirm that the polar space group $P12_11$ provides the most convincing explanation of our diffraction data. This space group is in contrast to the formerly suggested polar space group $Pb2_1m$, which does not allow (0 k l) reflections with odd k and integer l indices and is also not in accordance with the space group Pm suggested by Balédent *et al.* from single crystal synchrotron diffraction, which, however, allows all reflections with integer h, k, or l indices [55]. We suggest that the half-integer reflections appear in our neutron diffraction data and not in previous x-ray studies because of the different element-specific coherent scattering cross sections. For x-ray diffraction using an incident energy of 28 keV, the coherent cross section for O atoms is quite small. It is ≈70 times smaller than for Mn and ≈450 times smaller than for Tb. However, the coherent neutron scattering cross sections for these elements are comparable. It is conceivable that the noninteger reflections in our neutron diffraction data arise from coherent scattering from oxygen ions with similar but inequivalent positions. Such displacements could induce electrical dipole moments on the molecular level. However, as in the case of the a direction, they cancel out along the c direction and only contributions along the b axis add up to the final electric polarization.

Below the magnetic phase transition at $T_{\text{HT-ICM}} = 42$ K additional Bragg reflections appear which are not associated with nuclear reflections of the $P12_11$ space group. They can be attributed to magnetic diffraction and are described by the propagation vector of the type $\mathbf{k_M} = (\frac{1}{2}-\delta_x, 0, \frac{1}{4}+\delta_z)$ (see red right angles in Figs. 2 and 3). We have determined the propagation vectors directly from the diffraction maps obtained from the hl plane. At 40 K, magnetic "satellite" Bragg reflections appear at about (−1.51, 0, 2.28) and (−1.51, 0, 2.72) corresponding to $\mathbf{k_M}$ and $-\mathbf{k_M}$ of the star of the propagation vector for the $P12_11$ space group (see Table T3 in the Supplemental Material [57]). It should be noted that the centrosymmetric space group $Pbam$ used in previous publications provides four arms for the star of $\mathbf{k_M}$ which again can be reduced to two if k_x is 0.5 (see Table T4 in the Supplemental Material [57]). With respect to the magnetic selection rules, the magnetic Bragg peaks are in accordance with the crystallographic space group $P12_11$ (see text below Table T3 in the Supplemental Material [57]). Furthermore, the intensity of the magnetic reflections corresponding to each arm of the star of $\mathbf{k_M}$ may constitute the different projections of the magnetic moment perpendicular to the propagation vector [60]. Upon further cooling to the CM phase below $T_{\text{CM}} = 38$ K magnetic "satellite" Bragg reflections shift to (−1.50, 0, 2.25) and (−1.50, 0, 2.75), which corresponds to the commensurate propagation vector $\mathbf{k_M} = (\frac{1}{2}, 0, \frac{1}{4})$.

The temperature dependence of the peak positions in the q_h, q_k, and q_l directions and of the intensity of selected magnetic Bragg peaks, i.e., of (2.51, −4, 0.29), (−0.51, 2, 0.69), and (0.51, 4, −0.31) are shown in Fig. 6. The data were obtained by fitting Gaussian profiles to the peaks obtained from line cuts through the RSMs of the diffraction measurements in the ab, ac, and bc planes, respectively. The magnetic phase transitions occur at $T_{\text{HT-ICM}} = 42(1)$ K to the HT-ICM phase, at $T_{\text{CM}} = 38(1)$ K to the commensurate phase, and $T_{\text{LT-ICM}} = 24(1)$ K to the low-temperature incommensurate phase and are indicated by vertical dashed lines. The transition temperatures are in good agreement with previously published neutron diffraction data of Kobayashi *et al.* [28], Chapon *et al.* [22], and Wilkinson *et al.* [29]. However, Kobayashi *et al.* [28] observed a coexistence of the HT-ICM and CM phase from 37.8 to 36.5 K and of the CM and LT-ICM phase from 24.0 to 22.4 K. A similar result was obtained by Wilkinson *et al.* [29]. This was not seen in our experiment probably due to the coarser temperature steps used. At the onset of the magnetic order at $T_{\text{HT-ICM}} = 42(1)$ K magnetic Bragg peaks appear at ($h \pm 0.518$, k, $l \pm 0.28$) with h being an even integer and l an integer number. In the commensurate phase between 38(1) K and 24(1) K the magnetic propagation vector locks in at ($h \pm 0.5$, k, $l \pm 0.25$) and abruptly increases to ($h \pm 0.508$, k, $l \pm 0.309$) at the onset of the LT-ICM phase below $T_{\text{LT-ICM}} = 24(1)$ K. It increases upon further cooling and saturates at ($h \pm 0.513$, k, $l \pm 0.313$) below about 16 K. This is in good agreement with previously published data [22,28,29]. Our data do not provide any evidence for an incommensurability of the magnetic Bragg reflections in the CM phase. Remarkably, the intensities of the different magnetic Bragg peaks shown in Fig. 6 possess a distinct behavior. From 42 to 24 K, i.e., in the HT-ICM and in the CM phase, the intensities of all three magnetic Bragg peaks increase simultaneously. In this temperature range predominantly the Mn moments are ordered. At the transition to the LT-ICM phase at 24 K the intensities of the (2.51, −4, 0.29) and (−0.51, 2, 0.69) first decrease and then increase steeply upon further cooling while the (0.51, 4, −0.31) Bragg reflection increases continuously. However, the (−0.51, 2, 0.69) Bragg peak shows the strongest increase in intensity at lowest temperatures. According to Wilkinson *et al.* [29] it is most likely that the magnetic moments of Mn^{3+}/Mn^{4+} gain a c component at $T_{\text{LT-ICM}}$ reducing the magnetic component, especially of Mn^{3+} in the ab plane, and a bc cycloid is realized within a more complicated magnetic structure. Already about 10 K above the expected ordering temperature of the Tb^{3+} moments the magnetic exchange between the Mn and Tb moments leads to a polarization of the Tb spins. This has also been observed before in related materials such as $DyMnO_3$ [40], $TbVO_3$ [61], or $CeVO_3$ [62]. Wilkinson *et al.* determined that there are two distinct Tb sublattices in $TbMn_2O_5$, which possess a different increase in magnetic moment due to a different rotation of the Tb spins in the ab plane with temperature [29]. This can explain

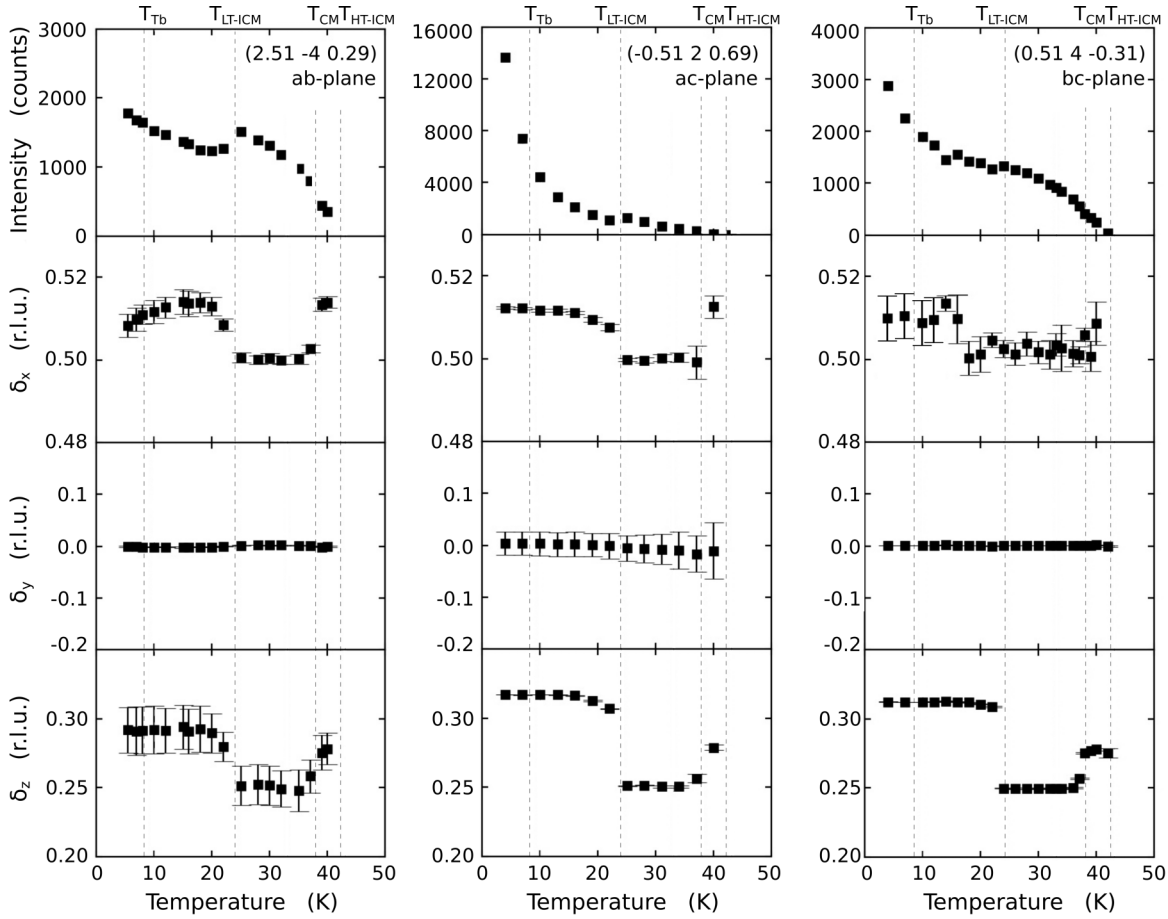

FIG. 6. Temperature dependence of the q_h, q_k, and q_l peak positions and peak intensities of selected magnetic Bragg reflections determined from the neutron diffraction measurements with the crystal being aligned in the *ab*, *ac*, and *bc* planes. Note that the q_l position for the measurement in the *ab* plane, the q_k position in the *ac* plane, and q_h in the *bc* plane were difficult to determine precisely since they appear out of the scattering plane. The different magnetic phase transitions are indicated by vertical dashed lines.

the observed differences in the temperature dependencies of the intensity of the different magnetic Bragg reflections, in particular the rapid increase at lowest temperatures due to the contribution again from the *ab* plane but from Tb^{3+} moments.

The increase in the peak intensities from 20 to 4 K is similar in form to the measured electric polarization [7,8], indicating that both phenomena are related to each other. The existence of a spin spiral in all magnetic phases of $TbMn_2O_5$ with a propagation direction along the *c* axis and close to quadrature phase steps has already been confirmed by previous diffraction experiments [29,32,37]. Due to the corresponding spin current the induced electric polarization is proportional to $\mathbf{S_i} \times \mathbf{S_j}$. This demonstrates that the leading mechanism for the magnetoelectric coupling in the LT-ICM phase is the spin current while, as discussed above, the dominating mechanism for the ME coupling in the CM phase is atomic displacements caused by exchange striction proportional to $\mathbf{S_i} \cdot \mathbf{S_j}$.

It should be noted that according to Petit *et al.* [27] and Sushkov *et al.* [63] the electromagnon is absent in the CM multiferroic phase of $TbMn_2O_5$ but increases abruptly in the LT-ICM phase. This suggests that the electromagnon is related to the spin-current mechanism while it does not couple to the electric polarization which arises from the magnetostriction in the CM phase. This provides valuable information on the origin of the electromagnon in multiferroics.

IV. CONCLUSIONS

In summary, our single crystal neutron diffraction experiments provide direct evidence of a lowering of the crystallographic symmetry for $TbMn_2O_5$ from the previously determined crystal structure *Pbam* to $P12_11$ through the observation of additional structural Bragg peaks at (h 0 l) and (0 k l) with h or k being an odd integer and l an integer number, and at (h 0 l) and (0 k l) positions with h or k being an integer and l a half-integer index. This structure exists already above the magnetic ordering temperature and does not change through all magnetic phases down to the lowest temperature. A noncentrosymmetric space group describing the precise crystallographic structure gives validity to the $\mathbf{S_i} \cdot \mathbf{S_j}$ based exchange-striction description of magnetoelectric coupling within the commensurate magnetic phase. In this scenario either the Mn^{3+} or Mn^{4+} ions move in the direction of the *ab*-plane zigzag units. This lifts the degeneracy of the magnetic exchange interactions J_3, which links the zigzag

chains, and J_4 within the Mn^{3+}-Mn^{4+}-Mn^{3+} zigzag units, and hence lowers the magnetic frustration and therefore stabilizes the magnetic structure [22]. The atomic displacements of the Mn^{3+}, Mn^{4+}, or Tb^{3+} ions generate electric polarizations on the atomic level, which cancel out in the *a* direction and accumulate along the *b* direction. Previously unobserved nuclear reflections at half positions in *Pbam* suggest a superstructure with a doubling of the unit cell along the *c* direction. The observation of these Bragg peaks only in neutron diffraction measurements suggests that these reflections correspond to a subtle displacement between otherwise inequivalent oxygen positions. This can create an electric polarization at the atomic level, which, however, cancels out along the *c* direction. In the LT-ICM phase the intensity of the magnetic Bragg reflections follows the intensity of the electric polarization. This suggests that the leading mechanism for the ME coupling in the LT-ICM phases is the spin-current model, which is caused by a spin cycloid in the *bc* plane with a propagation direction along the *c* axis. In this case the electric polarization is proportional to $\mathbf{S_i} \times \mathbf{S_j}$. These observations bring clarity to the previous issues regarding magnetoelectric coupling in $TbMn_2O_5$, which can also be readily generalized to the entire multiferroic RMn_2O_5 series.

ACKNOWLEDGMENTS

We would like to thank Dr. Juan Rodríguez-Carvajal from the Institut Laue-Langevin in Grenoble, France for the fruitful discussions about the program FULLPROF. This work was supported through the Australian Institute of Nuclear Science and Engineering Ltd (AINSE) and the Australian Research Council (ARC) through the funding of the Discovery Grants No. DP110105346 and No. DP160100545. The financial support from the German Research Foundation (DFG) through the Project No. B01 of the Collaborative Research Center SFB 1143 (project-id 247310070) and the Würzburg-Dresden Cluster of Excellence on Complexity and Topology in Quantum Matter ct.qmat (EXC 2147, project-id 390858490) is gratefully acknowledged. We thank the Australian Centre for Neutron Scattering for the allocation of neutron beam time on the instruments Joey and Wombat.

TABLE I. Extinction rules for the space groups of interest. The reflection conditions are listed in columns 3 and 4 (from Ref. [16]).

Space group	Point group	General	Special
Pbam	*mmm*	$0\,k\,l, k = 2n$ $h\,0\,l, h = 2n$ $h\,0\,0, h = 2n$ $0\,k\,0, k = 2n$	$hkl, h + k = 2n$ (for $2a, 2b, 2c, 2d, 4e, 4f$)
$Pb2_1m$	*m*2*m*	$0\,k\,l, k = 2n$ $0\,k\,0, k = 2n$	
*Pc*2*a*	*m*2*m*	$h\,k\,0, h = 2n$ $0\,k\,l, l = 2n$ $0\,0\,l, l = 2n$ $h\,0\,0, h = 2n$	
$P12_11$ (unique axis *b*)	2	$0\,k\,0, k = 2n$	
Pc	*m*	$0\,k\,l, k = 2n$ $0\,k\,0, k = 2n$	
Pm	*m*	No	
*P*2	2	No	
*P*1	1	No	

APPENDIX: SYMMETRY ANAYSIS OF THE DIFFERENT SPACE GROUPS

The extinction rules for the space groups of interest and the little group for $P12_11$, $\mathbf{k}_N = (0, 0, 1/2)$ and polar type distortions are given in Tables I and II, respectively. Decomposition of the representation: $\Gamma_{\mathrm{Dis},2a} = 3\Gamma_1 + 3\Gamma_2$.

TABLE II. Irreducible representations (IRREPs) of $P12_11$ for $\mathbf{k_N} = (0, 0, 1/2)$ and the basis for polar vector type distortions (for all atoms on the Wyckoff position 2*a*). The little group contains both of the symmetry elements belonging to $P12_11$ (from Ref. [16]).

IRREPs	Characters		Basis functions	
	1	2_1	x, y, z	$-x+1, y+1/2, -z+1$
Γ_1	1	1	(u, v, w)	$(u, -v, w)$
Γ_2	1	-1	(u, v, w)	$(-u, v, -w)$

[1] W. Eerenstein, N. D. Mathur, and J. F. Scott, Multiferroic and magnetoelectric materials, Nature (London) **442**, 759 (2006).
[2] R. Ramesh and N. A. Spaldin, Multiferroics: Progress and prospects in thin films, Nat. Mater. **6**, 21 (2007).
[3] J. F. Scott, Multiferroic memories, Nat. Mater. **6**, 256 (2007).
[4] S.-W. Cheong and M. Mostovoy, Multiferroics: A magnetic twist for ferroelectricity, Nat. Mater. **6**, 13 (2007).
[5] Y. Tokura, S. Seki, and N. Nagaosa, Multiferroics of spin origin, Rep. Prog. Phys. **77**, 076501 (2014).
[6] I. Kagomiya, S. Matsumoto, K. Kohn, Y. Fukuda, T. Shoubu, H. Kimura, Y. Noda, and N. Ikeda, Lattice distortion at ferroelectric transition of YMn_2O_5, Ferroelectrics **286**, 167 (2003).
[7] N. Hur, S. Park, P. A. Sharma, J. S. Ahn, S. Guha, and S-W. Cheong, Electric polarization reversal and memory in a multiferroic material induced by magnetic fields, Nature (London) **429**, 392 (2004).
[8] N. Hur, S. Park, P. A. Sharma, S. Guha, and S-W. Cheong, Colossal Magnetodielectric Effects in $DyMn_2O_5$, Phys. Rev. Lett **93**, 107207 (2004).
[9] H. Kimura, S. Kobayashi, S. Wakimoto, Y. Noda, and K. Kohn, Magnetically induced ferroelectricity in multiferroic compounds of RMn_2O_5, Ferroelectrics **354**, 77 (2007).
[10] Y. Noda, H. Kimura, M. Fukunaga, S. Kobayashi, I. Kagomiya, and K. Kohn, Magnetic and ferroelectric properties of multiferroic RMn_2O_5, J. Phys.: Condens. Matter **20**, 434206 (2008).
[11] P. G. Radaelli and L. C. Chapon, A neutron diffraction study of RMn_2O_5 multiferroics, J. Phys.: Condens. Matter **20**, 434213 (2008).
[12] K. Saito and K. Kohn, Magnetoelectric effect and low-temperature phase transitions of $TbMn_2O_5$, J. Phys.: Condens. Matter **7**, 2855 (1995).

[13] E. F. Bertaut, G. Buisson, A. Durif, J. Mareschal, M. C. Montmory, and S. Quezel-Ambrunaz, Compounds of rare earth oxides with transition metal oxides, Bull. Soc. Chim. Fr. **11**, 32 (1965).

[14] E. F. Bertaut, G. Buisson, S. Quezel-Ambrunanz, and G. Quezel, Structure magnetique et proprietes magnetiques de $BiMn_2O_5$, Solid State Commun. **5**, 25 (1967).

[15] S. C. Abrahams and J. L. Bernstein, Crystal structure of paramagnetic $DyMn_2O_5$ at 298 °K, J. Chem. Phys. **46**, 3776 (1967).

[16] *International Tables for Crystallography Vol. A1, Symmetry Relations between Space Groups*, edited by H. Wondratschek and U. Müller (Kluwer Academic Publishers, Dortrecht, 2004).

[17] G. Buisson, Ordre hélimagnétique du manganèse dans la série TMn_2O_5, Phys. Status Solidi A **16**, 533 (1973); Structures magnétiques sinusoïdales et hélicoïdales de la terre rare dans TMn_2O_5, **17**, 191 (1973).

[18] C. Wilkinson, F. Sinclair, P. P. Gardner, J. B. Forsyth, and B. M. R. Wanklyn, The antiferromagnetic structure of $DyMn_2O_5$ at 4.2 K, Solid State Phys. **14**, 1671 (1981).

[19] P. P. Gardner, C. Wilkinson, J. B. Forsyth, and B. M. Wanklyn, The magnetic structures of the rare-earth manganates $ErMn_2O$ and $TbMn_2O_5$, J. Phys. C: Solid State Phys. **21**, 5653 (1988).

[20] J. A. Alonso, M. T. Casais, M. J. Martínez-Lope, J. L. Martínez, and M. T. Fernández-Díaz, A structural study from neutron diffraction data and magnetic properties of RMn_2O_5 ($R =$ La, rare earth), J. Phys.: Condens. Matter **9**, 8515 (1997).

[21] I. Kagomiya, K. Kohn, and T. Uchiyama, Structure and ferroelectricity of RMn_2O_5, Ferroelectrics **280**, 131 (2002).

[22] L. C. Chapon, G. R. Blake, M. J. Gutmann, S. Park, N. Hur, P. G. Radaelli, and S-W. Cheong, Structural Anomalies and Multiferroic Behavior in Magnetically Frustrated $TbMn_2O_5$, Phys. Rev. Lett. **93**, 177402 (2004).

[23] G. R. Blake, L. C. Chapon, P. G. Radaelli, S. Park, N. Hur, S-W. Cheong, and J. Rodriguez-Carvajal, Spin structure and magnetic frustration in multiferroic RMn_2O_5 ($R =$ Tb, Ho, Dy), Phys. Rev. B **71**, 214402 (2005).

[24] C. Wang, G.-C. Guo, and L. He, First-principles study of the lattice and electronic structure of $TbMn_2O_5$, Phys. Rev. B **77**, 134113 (2008).

[25] S. Baidya, P. Sanyal, H. Das, B. Roessli, T. Chatterji, and T. Saha-Dasgupta, Understanding neutron scattering data in YMn_2O_5: An effective spin Hamiltonian, Phys. Rev. B **84**, 054444 (2011).

[26] J.-H. Kim, M. A. van der Vegte, A. Scaramucci, S. Artyukhin, J.-H. Chung, S. Park, S-W. Cheong, M. Mostovoy, and S.-H. Lee, Magnetic Excitations in the Low-Temperature Ferroelectric Phase of Multiferroic YMn_2O_5 Using Inelastic Neutron Scattering, Phys. Rev. Lett. **107**, 097401 (2011).

[27] S. Petit, V. Balédent, C. Doubrovsky, M. B. Lepetit, M. Greenblatt, B. Wanklyn, and P. Foury-Leylekian, Investigation of the electromagnon excitations in the multiferroic $TbMn_2O_5$, Phys. Rev. B **87**, 140301(R) (2013).

[28] S. Kobayashi, T. Osawa, H. Kimura, Y. Noda, N. Kasahara, S. Mitsuda, and K. Kohn, Neutron diffraction study of successive magnetic phase transitions in ferroelectric $TbMn_2O_5$, J. Phys. Soc. Jpn. **73**, 3439 (2004).

[29] C. Wilkinson, P. J. Brown, and T. Chatterji, Temperature evolution of the magnetic structure of $TbMn_2O_5$, Phys. Rev. B **84**, 224422 (2011).

[30] M. Deutsch, W. Peng, P. Foury-Leylekian, V. Balédent, S. Chattopadhyay, M. T. Fernandez-Diaz, T. C. Hansen, A. Forget, D. Colson, M. Greenblatt, M.-B. Lepetit, S. Petit, and I. Mirebeau, Pressure-induced commensurate order in $TbMn_2O_5$ and $DyMn_2O_5$: Influence of rare-earth anisotropy and $3d-4f$ exchange, Phys. Rev. B **98**, 024408 (2018).

[31] Y. Noda, H. Kimura, Y. Kamada, T. Osawa, Y. Fukuda, Y. Ishikawa, S. Kobayashi, Y. Wakabayashi, H. Sawa, N. Ikeda, and K. Kohn, Relation between ferroelectric and antiferromagnetic order in RMn_2O_5, Physica B **385-386**, 119 (2006).

[32] Y. Noda, H. Kimura, Y. Kamada, Y. Ishikawa, S. Kobayashi, Y. Wakabayashi, H. Sawa, N. Ikeda, and K. Kohn, Lattice modulation in YMn_2O_5 and $TbMn_2O_5$ studied by using synchrotron radiation x-rays, J. Korean Phys. Soc. **51**, 828 (2007).

[33] H. Kimura, S. Kobayashi, Y. Fukuda, T. Osawa, Y. Kamada, Y. Noda, I. Kagomiya, and K. Kohn, Spiral spin structure in the commensurate magnetic phase of multiferroic RMn_2O_5, J. Phys. Soc. Jpn. **76**, 074706 (2007).

[34] J.-H. Kim, S.-H. Lee, S. I. Park, M. Kenzelmann, A. B. Harris, J. Schefer, J.-H. Chung, C. F. Majkrzak, M. Takeda, S. Wakimoto, S. Y. Park, S-W. Cheong, M. Matsuda, H. Kimura, Y. Noda, and K. Kakurai, Spiral spin structures and origin of the magnetoelectric coupling in YMn_2O_5, Phys. Rev. B **78**, 245115 (2008).

[35] C. Vecchini, L. C. Chapon, P. J. Brown, T. Chatterji, S. Park, S-W. Cheong, and P. G. Radaelli, Commensurate magnetic structures of RMn_2O_5 ($R =$ Y, Ho, Bi) determined by single-crystal neutron diffraction, Phys. Rev. B **77**, 134434 (2008).

[36] S. Wakimoto, H. Kimura, M. Fukunaga, K. Nishihata, M. Takeda, K. Kakurai, Y. Noda, and Y. Tokura, Spin chirality and electric polarization in multiferroic compounds RMn_2O_5 ($R =$ Ho, Er), Physica B **404**, 2513 (2009).

[37] I. A. Zabokalo, S. V. Gavrilov, A. Sazonov, and V. Hutanu, Investigation of $TbMn_2O_5$ by polarized neutron diffraction, J. Phys.: Condens. Matter **30**, 205804 (2018).

[38] T. Kimura, T. Goto, H. Shintani, K. Ishizaka, T. Arima, and Y. Tokura, Magnetic control of ferroelectric polarization, Nature (London) **426**, 58 (2003).

[39] M. Kenzelmann, A. B. Harris, S. Jonas, C. Broholm, J. Schefer, S. B. Kim, C. L. Zhang, S.-W. Cheong, O. P. Vajk, and J. W. Lynn, Magnetic Inversion Symmetry Breaking and Ferroelectricity in $TbMnO_3$, Phys. Rev. Lett. **95**, 087206 (2005).

[40] N. Narayanan, P. J. Graham, N. Reynolds, F. Li, P. Rovillain, J. Hester, J. Kimpton, M. Yethiraj, G. J. McIntyre, W. D. Hutchison, and C. Ulrich, Subpicometer-scale atomic displacements and magnetic properties in the oxygen-isotope substituted multiferroic $DyMnO_3$, Phys. Rev. B **95**, 075154 (2017).

[41] H. Katsura, N. Nagaosa, and A. V. Balatsky, Spin Current and Magnetoelectric Effect in Noncollinear Magnets, Phys. Rev. Lett. **95**, 057205 (2005).

[42] I. A. Sergienko and E. Dagotto, Role of the Dzyaloshinskii-Moriya interaction in multiferroic perovskites, Phys. Rev B **73**, 094434 (2006).

[43] J. Koo, C. Song, S. Ji, J.-S. Lee, J. Park, T.-H. Jang, C.-H. Yang, J.-H. Park, Y. H. Jeong, K.-B. Lee, T. Y. Koo, Y. J. Park, J.-Y. Kim, D. Wermeille, A. I. Goldman, G. Srajer, S. Park, and S-W. Cheong, Non-Resonant and Resonant X-Ray Scattering Studies on Multiferroic $TbMn_2O_5$, Phys. Rev. Lett. **99**, 197601 (2007).

[44] C. Wang, G.-C. Guo, and L. He, Ferroelectricity Driven by the Noncentrosymmetric Magnetic Ordering in Multiferroic $TbMn_2O_5$: A First-Principles Study, Phys. Rev. Lett. **99**, 177202 (2007).

[45] S. Wakimoto, H. Kimura, Y. Sakamoto, M. Fukunaga, Y. Noda, M. Takeda, and K. Kakurai, Role of magnetic chirality in polarization flip upon a commensurate-incommensurate magnetic phase transition in YMn_2O_5, Phys. Rev. B **88**, 140403(R) (2013).

[46] S. Goshen, D. Mukamel, H. Shaked, and S. Shtiukman, Magnetic symmetry and ferroelectricity induced by antiferromagnetic transitions, J. Appl. Phys. **40**, 1590 (1969).

[47] H. C. Walker, F. Fabrizi, L. Paolasini, F. de Bergevin, J. Herrero-Martin, A. T. Boothroyd, D. Prabhakaran, and D. F. McMorrow, Femtoscale magnetically induced lattice distortions in multiferroic $TbMnO_3$, Science **333**, 1273 (2011).

[48] C. R. dela Cruz, F. Yen, B. Lorenz, S. Park, S.-W. Cheong, M. M. Gospodinov, W. Ratcliff, J. W. Lynn, and C. W. Chu, Evidence for strong spin-lattice coupling in multiferroic RMn_2O_5 (R = Tb, Dy, Ho) via thermal expansion anomalies, J. Appl. Phys. **99**, 08R103 (2006).

[49] C. R. dela Cruz, F. Yen, B. Lorenz, M. M. Gospodinov, C. W. Chu, W. Ratcliff, J. W. Lynn, S. Park, and S.-W. Cheong, Structural anomalies at the magnetic and ferroelectric transitions in RMn_2O_5 (R = Tb, Dy, Ho), Phys. Rev. B **73**, 100406(R) (2006).

[50] I. Kagomiya, K.-i. Kakimoto, and H. Ohsato, Precursor phenomenon on ferroelectric transition in multiferroic YMn_2O_5, J. Eur. Ceram. Soc. **30**, 255 (2010).

[51] C. Vecchini, A. Bombardi, L. C. Chapon, G. Beutier, P. G. Radaelli, S. Park, and S.-W. Cheong, Magnetically induced femtoscale strain modulations in $HoMn_2O_5$, Phys. Rev. B **89**, 125114 (2014).

[52] S. Matsumoto, M. Tanaka, I. Kagomiya, K. Kohn, and S. Nakamura, Mössbauer spectrum and spin structure of weakly ferroelectric YMn_2O_5 and $HoMn_2O_5$, Ferroelectrics **286**, 185 (2003).

[53] I. Kagomiya, S. Nakamura, S. Matsumoto, M. Tanaka, and K. Kohn, Mössbauer spectroscopy of ferroelectric YMn_2O_5, J. Phys. Soc. Jpn. **74**, 450 (2005).

[54] R. Valdés Aguilar, A. B. Sushkov, S. Park, S.-W. Cheong, and H. D. Drew, Infrared phonon signatures of multiferroicity in $TbMn_2O_5$, Phys. Rev. B **74**, 184404 (2006).

[55] V. Balédent, S. Chattopadhyay, P. Fertey, M. B. Lepetit, M. Greenblatt, B. Wanklyn, F. O. Saouma, J. I. Jang, and P. Foury-Leylekian, Evidence for Room Temperature Electric Polarization in RMn_2O_5 Multiferroics, Phys. Rev. Lett. **114**, 117601 (2015).

[56] B. M. Wanklyn, Flux growth of some complex oxide materials, J. Mater. Sci. **7**, 813 (1972).

[57] See Supplemental Material at http://link.aps.org/supplemental/10.1103/PhysRevB.105.214413 for additional information on the determination of the crystallographic and magnetic structure in $TbMn_2 2O_5$.

[58] A. J. Studer, M. E. Hagen, and T. J. Noakes, Wombat: The high-intensity powder diffractometer at the OPAL reactor, Physica B **385-386**, 1013 (2006).

[59] J. Rodríguez-Carvajal, Recent advances in magnetic structure determination by neutron powder diffraction, Physica B **192**, 55 (1993).

[60] B. Fåk, N. H. Van Dijk, and A. S. Wills, Comment on "Magnetic field effects on neutron diffraction in the antiferromagnetic phase of UPt_3", Phys. Rev. B **66**, 216401 (2002).

[61] M. Reehuis, C. Ulrich, P. Pattison, B. Ouladdiaf, M. C. Rheinstädter, M. Ohl, L. P. Regnault, M. Miyasaka, Y. Tokura, and B. Keimer, Neutron diffraction study of YVO_3, $NdVO_3$, and $TbVO_3$, Phys. Rev. B **73**, 094440 (2006).

[62] M. Reehuis, C. Ulrich, P. Pattison, M. Miyasaka, Y. Tokura, and B. Keimer, Crystal and magnetic structure of $CeVO_3$, Eur. Phys. J. B **64**, 27 (2008).

[63] A. B. Sushkov, R. Valdeś Aguilar, S. Park, S-W. Cheong, and H. D. Drew, Electromagnons in Multiferroic YMn_2O_5 and $TbMn_2O_5$, Phys. Rev. Lett. **98**, 027202 (2007).